

# Accepted manuscript doi: 10.1680/jgeot.17.p.118

---

## **Accepted manuscript**

As a service to our authors and readers, we are putting peer-reviewed accepted manuscripts (AM) online, in the Ahead of Print section of each journal web page, shortly after acceptance.

## **Disclaimer**

The AM is yet to be copyedited and formatted in journal house style but can still be read and referenced by quoting its unique reference number, the digital object identifier (DOI). Once the AM has been typeset, an 'uncorrected proof' PDF will replace the 'accepted manuscript' PDF. These formatted articles may still be corrected by the authors. During the Production process, errors may be discovered which could affect the content, and all legal disclaimers that apply to the journal relate to these versions also.

## **Version of record**

The final edited article will be published in PDF and HTML and will contain all author corrections and is considered the version of record. Authors wishing to reference an article published Ahead of Print should quote its DOI. When an issue becomes available, queuing Ahead of Print articles will move to that issue's Table of Contents. When the article is published in a journal issue, the full reference should be cited in addition to the DOI.

# Accepted manuscript doi: 10.1680/jgeot.17.p.118

---

**Submitted:** 03 May 2017

**Published online in ‘accepted manuscript’ format:** 14 March 2018

**Manuscript title:** Numerical Analysis of Field Geosynthetic-Reinforced Retaining Walls with Secondary Reinforcement

**Authors:** Y. Jiang\*, J. Han<sup>†</sup>, J. Zornberg<sup>‡</sup>, R. L. Parsons<sup>†</sup>, D. Leshchinsky<sup>§</sup> and B Tanyu<sup>||</sup>

**Affiliations:** \*Terracon Consultants, Inc., 2201 Rowland Ave, Savannah, Georgia 31404, USA; formerly University of Kansas, Kansas, USA; <sup>†</sup>Department of Civil, Environmental, & Architectural Engineering, the University of Kansas, Kansas, USA; <sup>‡</sup>The University of Texas at Austin, Austin, TX 78712, USA; <sup>§</sup>ADAMA Engineering, Inc., Clackamas, OR 97015, USA and <sup>||</sup>George Mason University, Fairfax, VA 22030, USA

**Corresponding author:** J. Han, Department of Civil, Environmental, & Architectural Engineering, the University of Kansas, Kansas, USA.

**E-mail:** jiehan@ku.edu

## **Abstract**

Geosynthetic-Reinforced Retaining (GRR) walls typically have vertical reinforcement spacing of 0.6 m, and this relatively large spacing has been known to cause comparatively high connection forces. To reduce this connection force, short geosynthetic reinforcement layers (referred to as secondary reinforcement layers) are installed between blocks where there are no primary reinforcement layers. This paper presents two-dimensional numerical simulations that were developed to analyze an instrumented GRR wall with secondary reinforcement layers in the field. A finite differential software was employed to develop the numerical model. In addition to the Mohr-Coulomb model, the Cap-Yield model based on the theory of hardening plasticity was used to represent the behavior of backfill. Inclinator casings, earth pressure cells, and strain gages were installed in the instrumented GRR walls to measure the facing deflections, lateral earth pressures, vertical earth pressures, and geogrid strains. The measured results and numerical predictions were compared and discussed, and reasonable agreement between these results was found. Compared to the measured results, the numerical predictions slightly underestimated the maximum wall facing deflections and vertical earth pressures, and slightly overestimated lateral earth pressures and strains in primary and secondary reinforcement layers. For comparison, a numerical model without secondary reinforcement was developed as well. This comparison revealed that the GRR wall with secondary reinforcement resulted in smaller facing deflections and maximum strains in primary reinforcement layers. Overall, the numerical analysis indicated that secondary reinforcement could provide clear benefits in improving the performance of GRR walls.

**Keywords:** deformation; field instrumentation; numerical modeling; reinforcement; retaining wall; stress analysis

## Introduction

Geosynthetic-reinforced retaining (GRR) walls have been used extensively in transportation and residential projects. Han (2015) identified the benefits of using such wall systems. The American Association of State Highway and Transportation Officials (AASHTO 2014) and the British Standards Institution (BS 8006-1:2010+A1:2016) have developed design guidelines for such GRR walls. The vertical spacing of geosynthetic reinforcement layers in a GRR wall is typically 0.6 m. This relatively large spacing can cause comparatively high connection forces near the back of the wall facing and even bulging of the wall facing. To mitigate such problems, additional short geosynthetic reinforcement layers (referred to as secondary reinforcement layers) are installed between primary geosynthetic reinforcement layers, as shown in Figure 1.

Analytical and experimental studies have been performed on GRR walls with secondary reinforcement layers (Leshchinsky 2000; Han and Leshchinsky 2006; Leshchinsky et al. 2014; and Jiang et al. 2015 and 2016). For example, Leshchinsky (2000) reported that the use of secondary reinforcement layers could mitigate the problems resulting from the relatively large vertical spacing of primary reinforcement layers in GRR walls. Han and Leshchinsky (2006) and Leshchinsky et al. (2014) used a limit equilibrium method to investigate the effect of secondary reinforcement on the behavior of GRR walls. Based on the results from centrifuge models and associated limit equilibrium analyses, Zornberg et al. (1998a, 1998b) concluded that secondary reinforcements played a significant role in the overall stability of geosynthetic-reinforced soil structures. In addition to analytical studies of GRR walls with secondary reinforcement layers, Jiang et al. (2015 and 2016) performed field tests to investigate the effect of secondary reinforcement on GRR wall performance. These results

confirmed that the secondary reinforcement could reduce the lateral deformation of the wall facing, the connection load, and the tensile load in the primary reinforcement layers.

Compared with analytical and experimental studies, numerical simulations can provide evaluations on a comparatively wider range of parameter values and, consequently, more comprehensive results. Extensive studies have been conducted to evaluate the behavior of GRR walls (e.g., Christopher et al. 1989; Ho and Rowe 1996; Ling and Leshchinsky 2003; Hatami and Bathurst 2006; Guler et al. 2007; Huang et al. 2009; Huang et al. 2011 and 2013; Mirmoradi and Ehrlich 2014; Yu et al. 2015; Zheng et al. 2016). In particular, Ling and Leshchinsky (2003) used two-dimensional finite element simulations to investigate the behavior of GRR walls. In their numerical model, a nonlinear hyperbolic model proposed by Duncan et al. (1980) was used to simulate the behavior of backfill. The numerical results showed that a decrease in the vertical reinforcement spacing reduced wall facing deflections and maximum tensile loads in reinforcement layers, but increased lateral pressure behind the wall. Similar to Ling and Leshchinsky (2003), Hatami and Bathurst (2006) evaluated the influence of backfill compaction and reinforcement type on the performance of GRR walls using the Fast Lagrangian Analysis of Continua (FLAC), a two-dimensional finite difference program. Using a three-dimensional finite difference program, FLAC3D, Huang et al. (2010) conducted numerical analyses to assess the behavior of a laterally loaded shaft constructed within a GRR wall. Based on the Huang et al. (2010) study, Huang et al. (2013) refined the numerical model by: (1) using the Cap-Yield model for backfill; (2) introducing interfaces between discrete facing blocks; and (3) considering compaction for backfill. The results from the refined model better matched those from field monitoring.

Although extensive numerical studies have been performed on GRR walls, very few have been performed on GRR walls with secondary reinforcement layers. Only Leshchinsky and

Vulova (2001) have investigated the influence of secondary reinforcement on failure modes of GRR walls. Their study illustrated that the inclusion of secondary reinforcement could reduce the connection load in the primary reinforcement, increase internal wall stability, and change the failure mode from reinforcement connection failure to compound failure.

In this study, a two-dimensional numerical model was developed using FLAC to analyze an instrumented GRR wall with secondary reinforcement layers. The Cap-Yield (CY) model was employed to simulate the behavior of backfill. The geosynthetic reinforcement was modeled as a linearly elastic-perfectly plastic material limited by its tensile strength, which was characterized as the yield strength. The block-block interface, block-backfill interface, backfill-geosynthetic reinforcement interface, compaction-induced stress, and construction procedures of GRR walls with secondary reinforcement were also considered in this study. The wall facing deflections, lateral earth pressures, vertical earth pressures, and strains in reinforcement layers from the field test and the numerical simulation are compared and discussed. For comparison, an additional numerical model was built to simulate a GRR wall without secondary reinforcement layers. In summary, while significant advances have been made regarding the use of numerical simulations in GRR walls, their use to investigate the effect of secondary reinforcements has been, at best, limited. This is certainly the case for numerical simulation that involved the comparison of numerical predictions against field monitoring results.

### **Brief Description of Instrumented GRR Wall**

The GRR wall evaluated in this study is located at Bonner Springs, Wyandotte County, Kansas, USA, and was constructed to support a new ramp for the Kansas Department of Transportation I-70/K-7 interchange project. The longitudinal length of the GRR wall is 353

m, of which a portion was designated as the test wall. Three wall sections were selected to be instrumented for field tests. In this paper, the test wall section with uniaxial geogrid as primary reinforcement and biaxial geogrid as secondary reinforcement was selected for the numerical simulation. This is because the instrumentation in this section was more comprehensive than that in the other two test wall sections.

Figure 2 shows a cross section of the instrumented wall. The wall was constructed on bedrock and had modular block facing. Four types of high-density polyethylene uniaxial geogrids were used as primary reinforcement and a polypropylene biaxial geogrid was used as secondary reinforcement. The lengths of the primary and secondary reinforcement layers were 18.0 to 18.3 m and 1.3 m, respectively. The backfill for the instrumented walls was gravel. The backfill was compacted with a lift thickness of 0.2 m. A light plate compactor was used to compact the backfill within 1 m behind the wall facing and a heavy roller compactor was used to compact the backfill at 1 m away from the wall facing. The primary geogrid layers were installed every two blocks (i.e., 0.4 m) in the lower third of the wall, and every three blocks (i.e., 0.6 m) in the upper two-thirds of the wall. A 4(h):1(v) backslope was constructed on the top of the wall.

The instrumentation was installed during the construction of the wall and its layout is shown in Figure 2. Wall facing deflections, lateral earth pressures at the back of the wall facing, vertical earth pressures at the bottom of the wall, and strains in primary and secondary reinforcement layers were measured during the construction. Details on the instrumentation can be found in Jiang et al. (2016).

## **Numerical Modeling**

### *Geometry and Boundary Conditions*

A two-dimensional (2D) numerical model was developed to analyze the instrumented wall. A 2D evaluation was selected because the wall length was approximately eight times larger than the length of the secondary reinforcement layers, which is typically required by a plane-strain condition. Figure 3 shows the mesh of the numerical model. The entire numerical model mainly included a foundation, embedment soil, wall facing, a reinforced soil zone, a retained soil zone, and a backslope. The foundation was 20 m thick and 72 m long. The foundation in front of the wall facing was extended to 36 m to minimize the boundary effects on the numerical simulations.

The height of the wall facing in the numerical model was 11.7 m, containing 58 stacked facing blocks and a wall cap that were 0.2 and 0.1 m in height, respectively. The width of the wall facing was 0.3 m. The reinforced soil zone was 18.3 m wide and 11.5 m high. The retained soil zone was 11.7 m high. To minimize boundary effects, the width of the retained soil zone was extended to 17.4 m. The embedment in front of the wall facing was constructed in two stages. The embedment in the numerical model was simulated as a right angle trapezoid. The height and upper width of the embedment were 2.2 and 6 m, respectively. The side slope of the embedment zone had a ratio of 3(h): 1 (v). The backslope was 5 m high starting from the back of the wall facing and extending upward with an approximate slope ratio of 4(h): 1 (v). As shown in Figure 3, the bottom of the model was fixed vertically and horizontally; and the left and right sides were fixed horizontally, but set to be free vertically.

Two constitutive models were used to simulate the behavior of the backfill: the Mohr-Coulomb (MC) model and the Cap-Yield (CY) model. The MC model represented a linearly elastic-perfectly plastic material with the Mohr-Coulomb failure criterion, and the parameters for this model are listed in Table 1.

The MC model as well as other soil constitutive models (e.g., a nonlinear hyperbolic model proposed by Duncan et al. 1980) have been used in the simulation of GRR walls (e.g. Hatami and Bathurst 2006, Huang et al. 2009, and Yu 2016). However, compared with those models, the CY model was developed based on the theory of hardening plasticity (Itasca 2011) and has the following capabilities: (1) to model the hardening behavior of volumetric strain under isotropic compression; (2) to simulate soil modulus decrease and plastic deformation subjected to shear loading; and (3) to exhibit dilative characteristics..

As shown in Figure 4, the CY model has two yield surfaces in  $p'-q$  space: (1) a cap yield surface and (2) a shear yield surface. An associated flow rule is used for the cap yield surface while a non-associated flow rule is adopted for the shear yield surface. Figure 5 shows the measured relationship between the volumetric strain and the isotropic compressive stress of the backfill, which was used to determine the parameters for the CY model. The details of the CY model are delineated in the FLAC manual of constitutive model (Itasca 2011)

The friction angle of the backfill was determined by three triaxial compression tests. As the numerical simulation of the instrumented wall was under a plane strain condition, a correlation for cohesionless soils recommended by Kulhway and Mayne (1990) was used to calculate the plane strain friction angle as follows:  $\phi_s = 1.12\phi_{tc} = 52^\circ$ , where  $\phi_s$  is the friction angle in the plane strain condition and  $\phi_{tc}$  is the friction angle from triaxial compression tests.

The dilation angle in the numerical simulation was determined using the equation given by Vermeer and De Borst (1984) for granular materials. The Cap-Yield surface parameter,  $\alpha$ , and the plastic strain coefficient,  $\beta$ , were calibrated by matching a stress-strain curve of the triaxial compression test at a confining stress of 200 kPa, as shown in Figure 6(a). Table 2 summarizes the CY model parameters for the backfill.

Figure 6 shows a comparison between the results from the triaxial compression tests and numerical predictions. The friction angle of a granular material depends on the confining stresses. In practice, however, a straight Mohr-Coulomb failure line, which is not dependent on confining stresses, is often used to characterize the shear strength of the material. This approach was also adopted in this study. It is not surprising that there are some differences between the experimental data and numerical results. However, in this study, comparisons of the two focused primarily on strain levels below 2%, as this was the strain level observed in the field. Fig. 6a shows very good agreement between the experimental and numerical results within this strain level.

The results from the isotropic compression test and the numerical simulation are also compared in Figure 7. A notable divergence can be seen between the results from the numerical simulation using the MC model and the isotropic compression test, whereas the results from the numerical simulation using the CY model agreed well with those from the isotropic compression test. The above comparisons demonstrate that the parameters for the CY model were successfully determined, calibrated, and verified.

The facing blocks and the foundation bedrock were modeled as linearly elastic materials and their properties are summarized in Table 1. The retained soil together with the backslope and embedment soils were modeled using the MC model to simulate their behavior and Table

1 presents their parameters. The parameters of the retained soil in this study were assumed to be same as those used in Huang et al. (2011) because these soils are from the same area.

### *Reinforcement Constitutive Models and Properties*

The numerical simulation in this study used strip elements for the reinforcement layers. The reinforcement was assumed to be a linearly elastic-perfectly plastic material, allowing for small deformations. The secant stiffness of the geogrid at 2% strain (1,000 hours creep strain) was selected as the constant stiffness for the numerical simulation. Tensile strain at failure was assumed to be 10%, and the yield strengths of the geogrids were the same as those provided by the manufacturer. Table 3 summarizes the parameters of reinforcement in the numerical simulation.

### *Interface Properties*

Four types of interfaces were considered in the numerical model: (1) the backfill-reinforcement interface; (2) the block-block interface; (3) the block-backfill interface; and (4) the block-embedment soil interface. These interfaces were modeled as linearly elastic-perfectly plastic with the MC failure criterion. The interface shear stress linearly increases with an increase in relative displacement and starts to yield at the maximum shear stress. Equation (1) gives the formula to calculate the maximum shear stress:

$$\tau_{\max} = c_{\text{int}} + \sigma'_n \cdot \tan \phi'_{\text{int}} \quad \text{Eq. (1)}$$

where  $c_{\text{int}}$  = interface cohesion;  $\sigma'_n$  = effective normal stress;  $\phi'_{\text{int}} = \tan^{-1}(c_{rf} \cdot \tan \phi) =$  friction angle of interface;  $c_{rf}$  = reduction factor; and  $\phi$  = friction angle of soil.

Table 4 summarizes the interface properties used in this study. The reduction factors  $c_{rf}$  of 0.67 and 0.84 were used to calculate the backfill-reinforcement interface friction angles for

the uniaxial geogrid and the biaxial geogrid, respectively. The dilation angle and cohesion of the backfill-reinforcement interface were assumed to be zero. A pullout test was used to calibrate the shear stiffness of the backfill-reinforcement interface.

The shear resistance between facing blocks mainly results from: (1) surface friction between facing blocks and (2) cohesion due to a connector serving as a shear key. The block-block interface properties were determined by referring to block-block shear test results in Hatami and Bathurst (2006). The properties of the interface between the leveling pad and the foundation were assumed to be the same as those of the block-block interface.

The friction angles of the block-backfill interface and the block-embedment interface were calculated using  $c_{rf} = 0.67$ . Their dilation angle and interface cohesion were assumed to be 8 degrees and 0 kPa, respectively. The interface normal and shear stiffness values were assumed to be the same as those used by Hatami and Bathurst (2006) because both studies used concrete modular blocks and granular materials for the backfill soils.

### *Modeling Procedures*

The numerical model simulated construction procedures as follows: (1) prior to wall construction, the foundation bedrock reached an equilibrium under gravity; (2) a layer of the wall facing, backfill and retained soil was placed in the numerical model; (3) primary and secondary reinforcement layers were installed and connected to the facing blocks; (4) corresponding interfaces were activated; (5) a vertical compaction stress was applied on the top of the reinforced soil; (6) the numerical model was solved to reach a new equilibrium; (7) Steps (2) to (6) were repeated up to the top of the wall; and (8) the backslope was constructed on the top of the wall.

The wall was built in lifts on a rigid foundation. To numerically simulate this construction procedure, a reinforced soil layer was activated without any settlement and compaction stresses were applied on top of this layer. The self-weight of the reinforced soil and the compaction stresses induced settlement after the numerical simulation reached equilibrium. After reaching equilibrium, the next reinforced soil layer was activated without settlement and compaction stresses were applied on the top of the new layer. The self-weight of the new layer and the new compaction stresses would induce settlements not only in the new layer, but also in the previous layer(s). This procedure was continued until all reinforced soil layers were placed. Since settlements of the previous layers accumulated under the placement of new layers, and the new layer did not have any settlement at the moment of placement, maximum settlements occurred at approximately the mid-height of the wall.

The numerical simulation was conducted using the small-strain mode in the software since the wall was under a working condition, and the measured wall facing deflections and reinforcement strains were comparatively small. A large-strain mode was used to analyze one case to verify the selection of the small-strain mode. The numerical results using the large-strain mode were almost identical to those using the small-strain mode; therefore, the selection of the small-strain mode was confirmed. Each reinforcement layer was connected to the facing block through a pin connection. The simulation of compaction stress is a challenge as there is no widely accepted method to do so. Hatami and Bathurst (2006) and Guler et al. (2007) modeled compaction stress by applying an 8-kPa distribution pressure on the top of each lift. Mirmoradi and Ehrlich (2014) modeled a compaction stress by applying an 8-kPa distribution stress at the top and bottom of each soil layer. Huang et al. (2013) simulated the effect of compaction stress by applying an additional lateral stress of 10 kPa to each lift via heavy compactor, or 8 kPa via light compactor. Yu et al. (2016) modeled

compaction stress by applying two 8- and 16-kPa distribution pressures on the top of each lift separately, for the same wall. The compaction stress in this study was modeled by applying an 8-kPa distribution pressure on the top of each lift. A more accurate simulation of compaction stress and investigation into the effect of the compaction stress level require further study, but they are beyond the scope of this study.

## **Numerical Results and Discussion**

### *Wall facing deflection*

The wall facing deflection from the numerical simulation was the deflection that occurred after the placement of the facing block. In other words, the deflection at a given wall height started at the moment when the wall construction reached that height. This approach has also been adopted in other studies, e.g., Hatami and Bathurst (2006) and Yu et al. (2016). In the following sections, the wall facing deflections are used for the convenience of presentation.

The wall facing deflections predicted by the numerical simulation and measured in the field test before and after construction of the backslope, are shown in Figures 8 (a) and (b), respectively. Both figures show that the deflections measured in the field test increased to the maximum and then decreased along the wall height. The deflections approached the maximum value at approximately the middle of the wall height. Although the maximum deflections predicted by the numerical simulation were slightly smaller than those from the field test, the deflections predicted by the numerical simulation captured the overall trend of the measured deflections. Guler et al. (2007), Huang et al. (2009), and Yu et al. (2016) also found similar trends along the wall height. After backslope construction, an increase in wall facing deflections can be observed in both the field test and the numerical simulation. This increase resulted from the weight of the backslope and the induced lateral earth pressure.

A comparison of wall facing deflections predicted by the numerical simulation using the MC and CY models can also be seen in Figure 8. Overall, the deflections predicted by the numerical simulation using the CY model were closer to the measured one than that using the MC model. Also, the CY model led to the larger wall facing deflections than the MC model. This is because the mobilized friction angle in the CY model was lower than the friction angle in the MC model. The soil yielded at the low strain level when the CY model was used. The difference in the deflections between the MC and CY models became larger after backslope construction because the soil modulus in the CY model further decreased due to shear stresses induced by the backslope, while the soil modulus in the MC model remained constant.

A GRR wall identical to that shown in Figure 3, but without secondary reinforcement layers was also numerically modeled using the CY model for comparison, as shown in Figure 8. It can be seen that the GRR wall without secondary reinforcement layers had larger wall facing deflections in the upper two-thirds of the wall height than that with secondary reinforcement layers. This demonstrates that the secondary reinforcement resulted in a reduction in wall facing deflections. This benefit increased after construction of the backslope. In Figure 8, this reduction in the deflections in the lower third of the wall is almost imperceptible, as the vertical spacing of the primary reinforcement is only 0.4 m, which is too close to show the benefits of the secondary reinforcement.

#### *Lateral earth pressures*

The numerical simulation predicted the lateral earth pressures before and after construction of the backslope as shown in Figure 9. For comparison, the lateral earth pressures predicted using the Rankine active earth pressure theory and the at-rest earth pressure are also shown in

Figure 9. The lateral earth pressures predicted by the numerical simulation above the embedment zone increased approximately linearly with depth and were close to the Rankine active earth pressures. In the numerical simulation, the lateral earth pressure from the top of the embedment zone to the bottom of the wall increased substantially, and then approached the at-rest earth pressure at the bottom of the wall. This is because the embedment soil in front of the wall restricted the development of wall facing deflections within the embedment zone so that the lateral earth pressure within the embedment zone was close to the at-rest earth pressure. Above the embedment zone, the lateral earth pressures predicted by the numerical simulation showed a reasonable agreement with those from the field test. Figure 9 shows that the measured lateral earth pressures were comparatively large near the top of the wall, likely because the wall facing deflections were comparatively small near the wall top due to the later placement of fill materials. As a result, the active lateral earth pressures were not fully mobilized at this location. Also, the measured lateral earth pressure at the locations within the embedment deviated from the numerical result and at-rest earth pressure. This deviation may result from the soil arching effect due to the stiffness difference between the wall facing and the backfill, which resulted in a lower vertical stress.

The results from the field test and numerical simulation showed the increased pressures due to construction of the backslope. Figure 9 also shows that the lateral earth pressures predicted using the CY model are almost same as those using the MC model. The pressures predicted for the GRR wall without secondary reinforcement were nearly the same as those for the GRR wall with secondary reinforcement, and therefore the lateral earth pressures predicted for the wall without secondary reinforcement are not shown in Figure 9.

*Vertical earth pressures*

Figure 10 shows the distributions of vertical earth pressure at the bottom of the wall from the field test and the numerical simulation as well as those calculated using the simplified methods. The vertical pressures from the numerical simulation decreased at the back of the wall facing due to the soil arching effect between the wall facing and the backfill soil. The reinforced soil behind the back of the wall facing was subjected to upward friction because the reinforced soil settled more than the wall facing, which then reduced the vertical earth pressure at the bottom of the wall. The overburden stress calculated by the simplified method is the unit weight of the soil multiplied by the depth. The trapezoid stress was calculated by considering the reinforced zone as a rigid body subjected to a lateral earth pressure from the retained soil. However, the effect of friction was not considered in the simplified methods to calculate the trapezoid and overburden stresses. After the sudden drop, the vertical earth pressure at the bottom of the wall reached a relatively constant value before construction of the backslope and then gradually increased after the construction of the backslope. As indicated by Jiang et al. (2016), the second measured point from the left was not reliable, potentially due to the malfunction of this earth pressure cell. Although the vertical earth pressures predicted by the numerical simulation slightly underestimated those measured from the field test, the predicted and measured pressures reasonably corresponded, as did the calculated trapezoid stresses.

Figure 10 also shows that the CY model predicted slightly lower vertical pressures than the MC model. Since the vertical earth pressures predicted at the bottom of the wall were almost the same for the GRR walls with and without secondary reinforcement, the pressures for the GRR wall without secondary reinforcement are not shown in Figure 10.

*Strains in reinforcement layers*

Figure 11 presents the strain distribution in the primary reinforcement layers at five instrumented layers (see Figure 2) after the construction of the backslope. Positive strains indicate tension in the reinforcement layers, while negative strains indicate compression. The predicted strains at each instrumented layer quickly decreased from the back of the wall facing and gradually decreased to zero. Both field test and numerical simulation show negative strains appeared in the rear segment of the primary reinforcement layers because the reinforced soil was compressed by lateral earth pressure from the retained soil. Overall, the numerically predicted strains in the primary reinforcement layers reasonably tracked the measured strain distribution from the field test. In addition, the maximum tensile strain distribution along the wall height matched well with the wall facing deflection distribution. Also, the tensile strains predicted in the primary reinforcement layers using the MC model were smaller than those using the CY model.

Figure 11 also shows the strains predicted in the primary reinforcement layers using the CY model for the GRR wall without secondary reinforcement. The maximum tensile strain occurred at the connection and followed by a rapid decrease in the GRR wall without secondary reinforcement. However, a different distribution was found in the wall with secondary reinforcement. For example, the maximum tensile strains in Layers 2, 3, and 4 occurred at the end of the zone reinforced with secondary reinforcement layers. Compared with the GRR wall without secondary reinforcement, the tensile strain distribution of the primary reinforcement in the GRR wall with the secondary reinforcement was altered within the secondary reinforcement zone except for Layer 1. The tensile strain at the connection was reduced by the secondary reinforcement layers. The placement of secondary reinforcement layers could be considered a reduction of reinforcement spacing. Since the secondary

reinforcement carried tensile forces near the wall facing, the forces required for the primary reinforcements to maintain stability of the wall facing became smaller. As a result, the secondary reinforcements resulted in a reduction in the connection stresses in the primary reinforcement.

Figure 12 presents the distribution of tensile strain in the secondary reinforcement layers after construction of the backslope. Overall, the strains predicted at each instrumented layer decreased quickly behind the back of the wall facing. The maximum strains in the secondary reinforcement calculated by the numerical simulation occurred at the connection. The measured tensile strains near the wall facing were lower than the calculated ones from the numerical simulation because the middle portion of the connector during the construction might not be in tight contact with the block and the measured strains in the reinforcement near the wall facing were relatively low. The predicted tensile strains away from the wall facing from the numerical simulation were close to the measured ones. Overall, there was a reasonable agreement between the strains predicted by the numerical simulation and those measured in the field test. Again, the tensile strains predicted using the CY model were larger than those in the MC model.

#### *Stresses in primary reinforcement layers*

Figure 13 shows the distribution of maximum tensile stresses in the primary reinforcement layers from the field test and the numerical simulation, after the construction of the backslope. As shown in Figure 13, the maximum tensile stress from the numerical simulation increased with depth and reached its greatest value at approximately the middle of the wall. Thereafter, the maximum tensile stress decreased with depth toward the bottom of the wall. The decrease in the maximum tensile stress in the primary reinforcement layer in the lower

part of the wall was due to two reasons: (1) the vertical spacing of the primary reinforcement became smaller and (2) the embedment limited the development of wall facing deflection. The numerically predicted maximum tensile stress tracked the maximum tensile stress distribution along the depth of the wall from the field test, although the values from the numerical simulation were slightly higher. Furthermore, the maximum tensile stresses in the primary reinforcement layers were higher using the CY model than the MC model because of the decreased soil modulus in the CY model.

For comparison, the distribution of maximum tensile stresses for the GRR wall without secondary reinforcement is also presented in Figure 13. The maximum tensile stresses for this case were higher than those for the wall with secondary reinforcement. This result indicates again that the secondary reinforcement reduced the maximum tensile stresses in the primary reinforcement layers. The AASHTO simplified method (AASHTO 2014) was employed to calculate the maximum tensile stresses in the primary reinforcement layers, as shown in Figure 13. Two friction angles,  $47^\circ$  and  $52^\circ$ , were used in the calculation for the following reasons: (1) a friction angle of  $47^\circ$  was obtained from triaxial compression tests, and the AASHTO simplified method recommends the use of the shear strength from triaxial compression tests; and (2) a friction angle of  $52^\circ$  was converted for the plane strain condition and was used in the numerical simulation. As shown in Figure 13, in the upper two-thirds of the wall, the maximum tensile stresses calculated using the AASHTO simplified method captured the trend of maximum tensile stresses from the numerical simulation; and the maximum tensile stresses calculated using the friction angle of  $52^\circ$  agreed well with those from the numerical simulation for the wall without secondary reinforcement. However, in the lower third of the wall, the maximum tensile stresses from the numerical simulation decreased with depth, while the maximum tensile stresses calculated using the AASHTO

simplified method increased with the depth. This result can be attributed to the conservatism of the AASHTO simplified method, as it ignores the effect of toe resistance, which results in the reduced maximum tensile stress.

It should be noted that only a few secondary reinforcement layers in the lower portion of the wall intercept the potential Rankine failure surface. In the field study as well as the numerical simulation, the wall was embedded and the soil in front of the wall minimized wall movement and prevented the possible development of this surface. As a result, the measured earth pressures in the lower portion of the wall were close to the at-rest lateral earth pressure values. The numerical results show that the secondary reinforcements in the lower portion of the wall did not reduce the tensile stresses in the primary reinforcement layers. The effect of secondary reinforcements on the tensile stresses in the primary reinforcements would be more significant if the wall had not been embedded and had been close to its limit state.

The design procedure for considering the influence of the secondary reinforcement on the tensile stress in the primary reinforcement is provided in the research report by Jiang et al. (2015).

## **Conclusions**

This study performed two-dimensional numerical simulations to analyze the results from an instrumented geosynthetic-reinforced retaining (GRR) wall constructed with secondary reinforcement layers. Cap-Yield (CY) model was used to simulate the behavior of backfill. Parameters for the CY model were successfully determined, calibrated and verified by triaxial compression and isotropic compression tests. Wall facing deflections, vertical earth pressures, lateral earth pressures, strains in primary and secondary reinforcement layers, and maximum tensile stresses from the field test were compared with the predictions from the

numerical simulation. For comparison, the same GRR wall without secondary reinforcement layers was also numerically modeled. The following conclusions can be drawn:

- (1) Overall, the numerical simulation was found to adequately predict the behavior of GRR wall with secondary reinforcement layer in terms of the distribution of wall facing deflections, lateral and vertical earth pressures, strains in reinforcement layers.
- (2) The numerical simulation using the CY model resulted in a better agreement with the field test results in aspects of wall facing deflections than using the MC model. The numerical simulation using the CY model predicted larger wall facing deflections, vertical earth pressures, and strains in reinforcement layers than using the MC model; while the both models produced almost same results of lateral and vertical earth pressures.
- (3) The wall facing deflections for the wall without secondary reinforcement layers were found to be larger than those for the wall with secondary reinforcement layers. This result demonstrates that the use of secondary reinforcement leads to the reduced wall facing deflections. However, the benefit of reduced wall facing deflection from secondary reinforcement was diminished by the closer vertical spacing of the primary reinforcement layers.
- (4) The lateral earth pressures predicted by the numerical simulation above the embedment were found to be well represented by the Rankine active earth pressures. However, the lateral earth pressures predicted by the numerical simulation below the top of the embedment zone increased substantially, and then approached at-rest earth pressure at the bottom of the wall.
- (5) Overall, the tensile strains in the primary reinforcement layers using the MC model were smaller than those using the CY model, especially at the locations close to the

wall facing. The tensile strains in the primary reinforcement layers at the connection was reduced by the secondary reinforcement layers.

- (6) The numerically-predicted maximum tensile stress tracked the maximum tensile stress distribution from the field test along the depth of the wall. The maximum tensile stress predicted using the AASHTO simplified method agreed well with results from the numerical simulation for a GRR wall without secondary reinforcement layers in the upper two-thirds of the wall. However, the maximum tensile stress calculated in the numerical simulation in the lower third of the wall decreased with depth, while the maximum tensile stress calculated using the AASHTO simplified method increased with depth. This can be attributed to the conservatism of the AASHTO simplified method, as it ignores the effect of toe resistance, which results in the reduced maximum tensile stress.

### **Acknowledgements**

This study was sponsored by the Kansas Department of Transportation (KDOT). The Geosynthetic Institute provided the first author a GSI fellowship on this study. The authors would like to thank all the sponsors and appreciate the support from Mr. James J. Brennan, the former chief geotechnical engineer of KDOT.

## Notation

- $c_{\text{int}}$  interface cohesion  
 $c_{rf}$  reduction factor  
 $p'$  mean effective stress  
 $q$  deviatoric stress  
 $\sigma'_n$  effective normal stress  
 $\phi$  friction angle of soil  
 $\phi'_{\text{int}}$  friction angle of interface  
 $\phi_s$  friction angle in the plane strain condition  
 $\phi_{ic}$  friction angle from triaxial compression tests  
 $\tau_{\text{max}}$  maximum shear stress of interface

## References

- AASHTO. (2014). LRFD bridge design specifications. 7th ed., Washington, DC.
- BSI. (2016). BS 8006-1:2010+A1:2016 Code of practice for strengthened/reinforced soils and other fills. London, UK: BSI.
- Christopher, B.R., Gill, S.A., Giroud, J.P., Juran, I. Scholsser, F., Mitchell, J.K. & Dunnicliff, J. (1989). Reinforced soil structures, Volume II. Summary of research and systems information. *Report No. FHWA-RD-89-043*, Federal Highway Administration, Washington DC, November 1989, 287 p.
- Duncan, J. M., Byrne, P. M., Wong, K. S. & Mabry, P. (1980). Strength, stress-strain and bulk modulus parameters for finite element analyses of stresses and movements in soil masses. *Rep. No. UCB/GT/80-01*, Dept. of Civil Engineering, Univ. of California, Berkeley, CA.
- Guler, E., Hamderi, M. & Demirkan, M. M. (2007). Numerical analysis of reinforced soil-retaining wall structures with cohesive and granular backfills. *Geosynthetics International*, 14, No. 6, 330-345.

- Han, J. (2015). *Principles and Practice of Ground Improvement*, John Wiley & Sons, Hoboken, New Jersey, USA, ISBN: 978-1-118-25991-7, June, 432p
- Han, J. & Leshchinsky, D. (2006). General analytical framework for design of flexible reinforced earth structures. *J. Geotech. Geoenviron. Eng.* 132, No. 11, 1427-1435.
- Hatami, K. & Bathurst, R.J. (2006). Numerical model for reinforced soil segmental walls under surcharge loading." *J. Geotech. Geoenviron. Eng.* 132, No. 6, 673-684.
- Ho, S.K. & Rowe, R.K. (1996). Effect of wall geometry on the behaviour of reinforced soil walls. *Geotextiles and Geomembranes* 14, No. 10, 521-541.
- Huang, B.Q., Bathurst, R.J. & Hatami, K. (2009). Numerical study of reinforced soil segmental walls using three different constitutive soil models. *J. Geotech. Geoenviron. Eng.* 135, No. 10, 1486-1498.
- Huang, J., Parsons, R.L., Han, J. & Pierson, M.C. (2011). Numerical analysis of a laterally loaded shaft constructed within an MSE wall. *Geotextiles and Geomembranes* 29, No. 3, 233-241.
- Huang, J., Han, J., Parsons, R.L. & Pierson, M.C. (2013). Refined numerical modeling of a laterally-loaded drilled shaft in an MSE wall. *Geotextiles and Geomembranes* 37, 61-73.
- Itasca Consulting Group. (2011). *FLAC: Fast Lagrangian Analysis of Continua*, version 7.0, Itasca Consulting Group, Inc., Minneapolis, Minn.
- Jiang, Y., Han, J., Parsons, R.L. & Cai, H. (2015). Field monitoring of mse walls to investigate secondary reinforcement effects. *Final Report, KDOT C1968*, Kansas Department of Transportation.
- Jiang, Y., Han, J., Parsons, R.L. & Brennan, J.J. (2016). Field instrumentation and evaluation of modular-block MSE walls with secondary geogrid layers. *J. Geotech. Geoenviron. Eng.*, [http://dx.doi.org/10.1061/\(ASCE\)GT.1943-5606.0001573](http://dx.doi.org/10.1061/(ASCE)GT.1943-5606.0001573), 05016002.

- Kulhawy, F.H. & Mayne, P.W. (1990). Manual on estimating soil properties for foundation design. *EPRI-EL-6800* Electric Power Research Inst., Palo Alto, CA, August 1990, 380p.
- Leshchinsky, D. (2000). Alleviating connection load. *Geotechnical Fabrics Report*, 34-39
- Leshchinsky, D. & Vulova, C. (2001). Numerical investigation of the effects of geosynthetic spacing on failure mechanisms of MSE block walls. *Geosynthetics International* 8, No. 4, 343-365.
- Leshchinsky, D., Kang, B.J., Han, J. & Ling, H.I., (2014). Framework for limit state design of geosynthetic-reinforced walls and slopes. *Trans. Infrac. Geotech.* 1, No. 2, 129-164.
- Ling, H.I. & Leshchinsky, D. (2003). Finite element parametric study of the behavior of segmental block reinforced-soil retaining walls. *Geosynthetics International* 10, No. 3, 77-94.
- Mirmoradi, S.H. & Ehrlich, M. (2014). Numerical evaluation of the behavior of grs walls with segmental block facing under working stress conditions. *J. Geotech. Geoenviron. Eng.* 141, No. 3, 1-8.
- NTPEP. (2011). Laboratory evaluation of geosynthetic reinforcement. *National transportation product evaluation program*, NTPEP Report 8507.4, Washington D.C., USA: American Association of State Highway and Transportation Officials.
- Vermeer, P. A. & de Borst, R. (1984). Non-associated plasticity for soils, concrete and rock. *Heron* 29, No. 3, 1-64.
- Yu, Y., Bathurst, R.J. & Allen, T.M. (2016). Numerical modelling of the SR-18 geogrid reinforced modular block retaining walls. *J. Geotech. Geoenviron. Eng.* 142, No. 5, 10.1061/(ASCE)GT.1943-5606.0001438, 04016003.
- Zheng, Y. & Fox, P. (2016). Numerical investigation of geosynthetic-reinforced soil bridge abutments under static

loading. *J. Geotech. Geoenviron. Eng.* 142, No. 5, 10.1061/(ASCE)GT.1943-5606.0001452, 04016004.

Zornberg, J.G., Sitar, N. & Mitchell, J.K. (1998). "Performance of Geosynthetic Reinforced Slopes at Failure." *J. Geotech. Geoenviron. Eng.*, ASCE, Vol. 124, No. 8, pp. 670-683.

Zornberg, J.G., Sitar, N. & Mitchell, J.K. (1998). "Limit Equilibrium as Basis for Design of Geosynthetic Reinforced Slopes." *J. Geotech. Geoenviron. Eng.*, ASCE, Vol. 124, No. 8, pp. 684-698.

**Table 1.** Parameters in the numerical model

Material	Constitutive model	Unit weight (kN/m <sup>3</sup> )	Young's modulus (MPa)	Poisson's ratio	Cohesion (kPa)	Friction angle (°)	Dilation angle (°)
Backfill	Mohr-Coulomb	18.1	20	0.2	0	52	8
Retained soil/ Backslope/ Embedment	Mohr-Coulomb	16.8/20.0 <sup>1</sup>	20	0.3	1	34	0
Foundation bedrock	Linearly elastic	20.0	2000	0.2	0	0	0
Block facing	Linearly elastic	15.0	2000	0.25	-	-	-

Note:<sup>1</sup>The unit weight of backslope was assumed to be 20.0 kN/m<sup>3</sup>.

**Table 2.** Parameters for the Cap-Yield model of the backfill

Parameters	Unit	Value
Unit weight, $\gamma$	kN/m <sup>3</sup>	18.1
Cap-yield surface parameter, $\alpha$	-	1.5
Friction angle, $\phi$	°	52
Dilation angle, $\psi$	°	8
Multiplier, $R$	-	6.2
Plastic strain coefficient, $\beta$	-	0.5
Reference elastic tangent shear modulus, $G_{ref}^e$	kPa	32500
Reference bulk modulus, $K_{ref}^{iso}$	kPa	6971
Reference pressure, $P_{ref}$	kPa	100
Poisson's ratio, $\nu_{ur}$	-	0.2
Cohesion, $c$	kPa	0
Power, $m$	-	0.52
Failure ratio, $R_f$	-	0.9

**Table 3.** Parameters of geogrid in numerical modelling

Materials	Structure element type	Constitutive model	Secant stiffness at 2%, $J_{@2\%}$ (kN/m)	Yield strength (kN/m)	Tensile failure strain (%)
UX1	Strip	Linearly elastic and perfectly plastic	360	58	10
UX2			407	70	10
UX3			637	114	10
UX4			860	144	10
BX			330*	19	10

Note: \* stiffness in the cross-machine direction

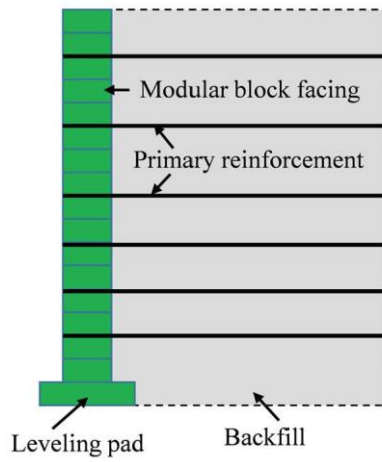
**Table 4.** Interface parameters

Interface	Friction angle (°)	Dilation angle (°)	Cohesion (kPa)	Normal stiffness, $k_n$ (MN/m/m)	Shear stiffness, $k_s$ (MN/m/m)
Backfill-reinforcement	40/47 <sup>1</sup>	0	0	-	6.5
Block-block	57	0	46	1000	40
Block-backfill	40	8	0	100	1
Block-embedment	28	0	0	100	1

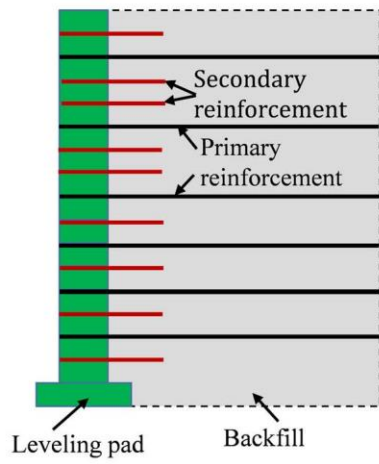
Note: <sup>1</sup>40° is for uniaxial geogrid, and 47° is for biaxial geogrid.

**List of Figure Captions**

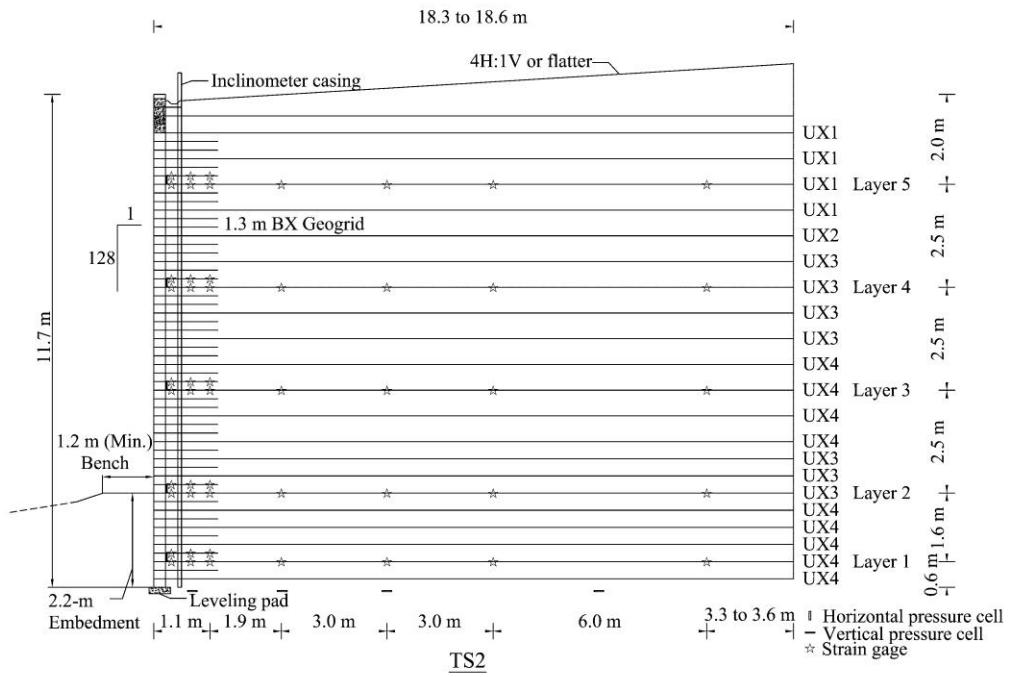
- Figure 1. Cross section of GRR walls: (a) without secondary reinforcement layers; (b) with secondary reinforcement layers
- Figure 2. Cross section of instrumented wall (Jiang et al. 2016, with permission from ASCE)
- Figure 3. Mesh of the numerical model
- Figure 4. Yield surfaces of the CY model in  $p'$ - $q$  space
- Figure 5. Power function for the relationship between volumetric strain and isotropic compressive stress
- Figure 6. Numerical simulation of triaxial compression tests on the backfill using MC model and CY models: (a) stress-strain relationship; and (b) volumetric-axial strain relationship
- Figure 7. Numerical simulation of isotropic compression test on the backfill using MC model and CY models: (a) stress-strain relationship; and (b) volumetric-axial strain relationship
- Figure 8. Wall facing deflections: (a) before construction of the backslope; (b) after construction of the backslope
- Figure 9. Lateral earth pressure: (a) before construction of the backslope; (b) after construction of the backslope
- Figure 10. Vertical earth pressure: (a) before construction of the backslope; (b) after construction of the backslope
- Figure 11. Distribution of strains in primary reinforcement layers: (a) Layer 1; (b) Layer 2; (c) Layer 3; (d) Layer 4; (e) Layer 5
- Figure 12. Distribution of strains in secondary reinforcement layers: (a) Layer a; (b) Layer b; (c) Layer c; (d) Layer d; (e) Layer e
- Figure 13. Distribution of maximum tensile stress



jiangfig01a

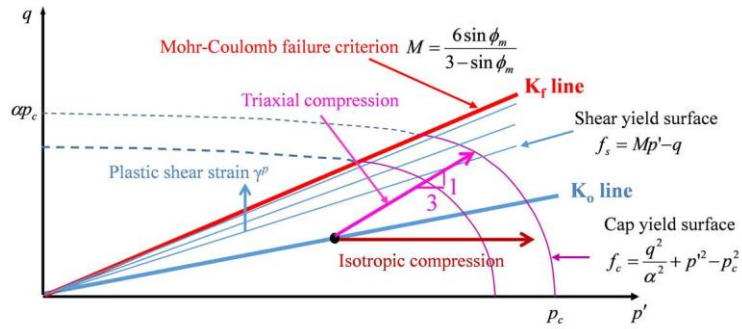


jiangfig01b

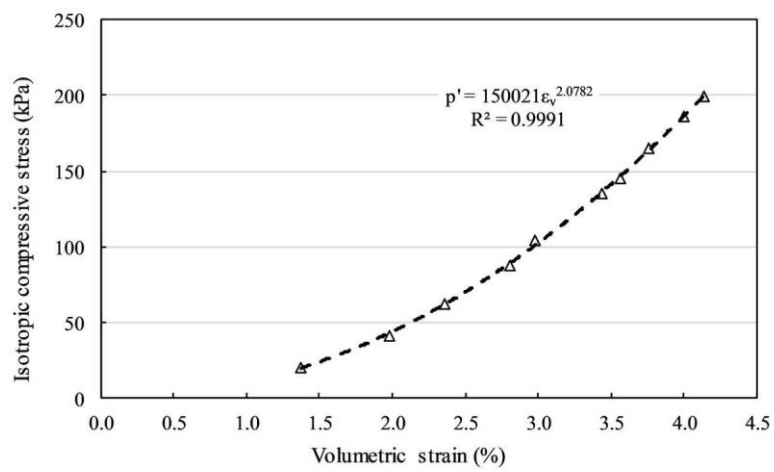


jiangfig02

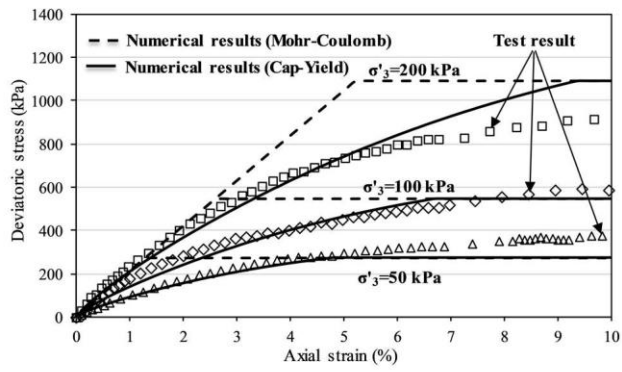




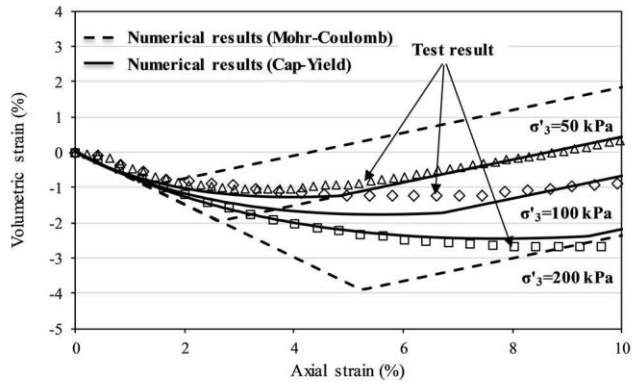
jiangfig04



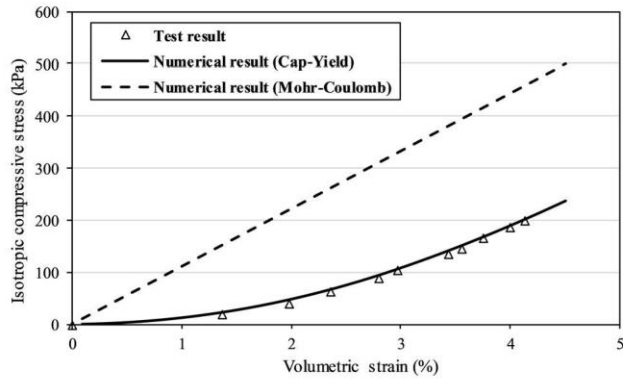
jiangfig05



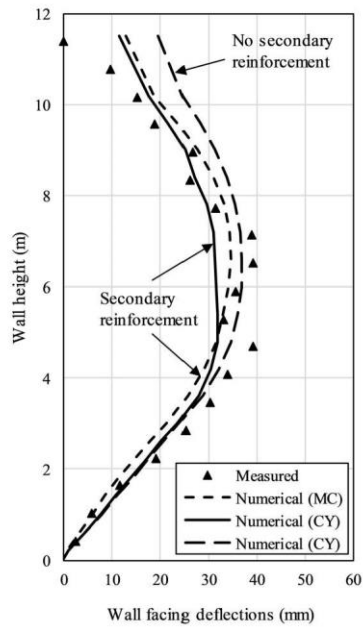
jiangfig06a



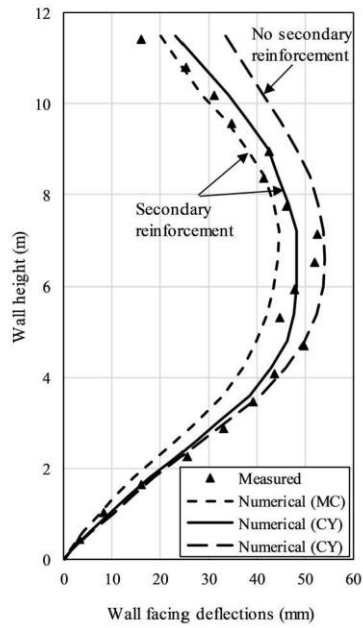
jiangfig06b



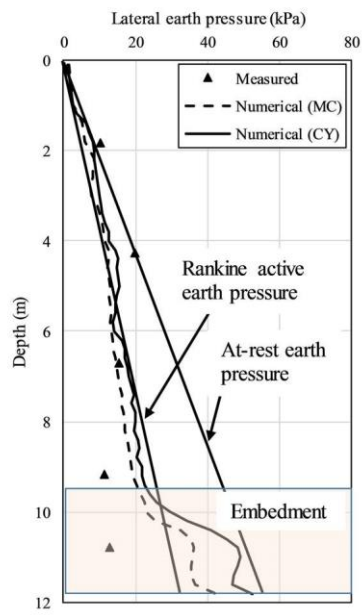
jiangfig07



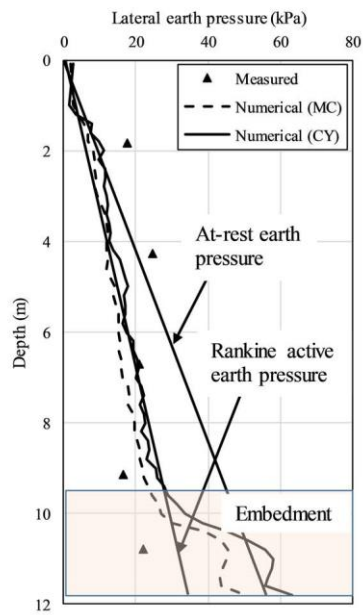
jiangfig08a



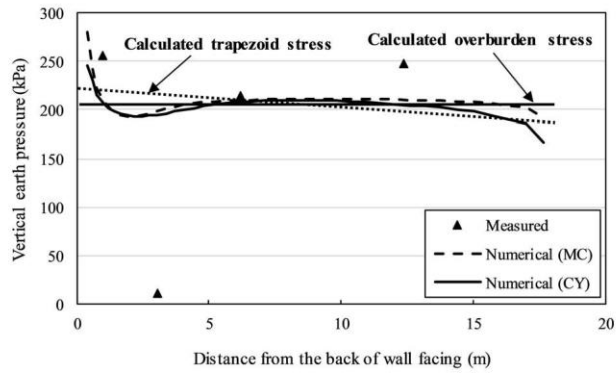
jiangfig08b



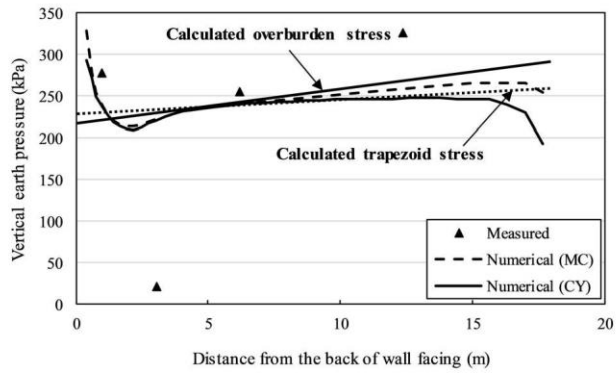
jiangfig09a



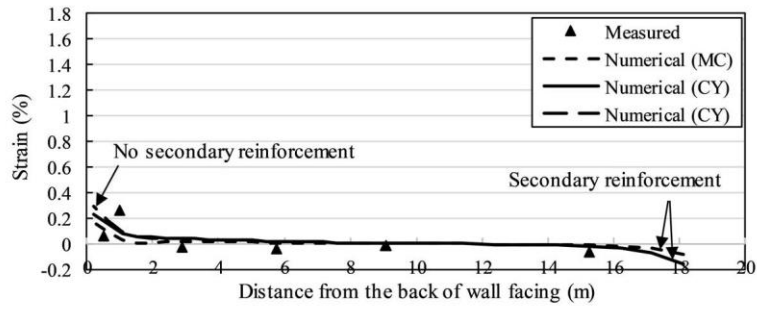
jiangfig09b



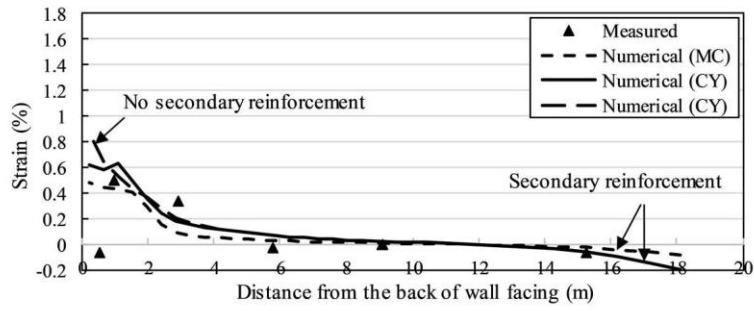
jiangfig10a



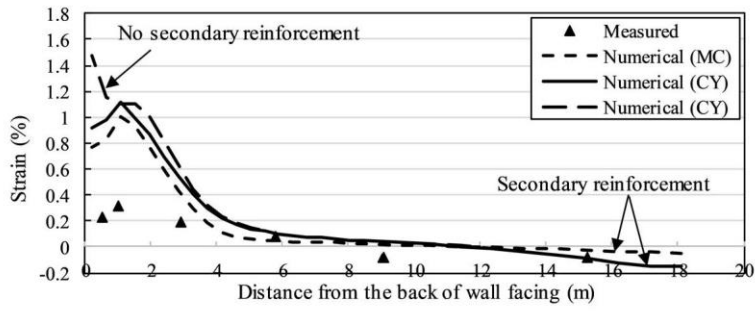
jiangfig10b



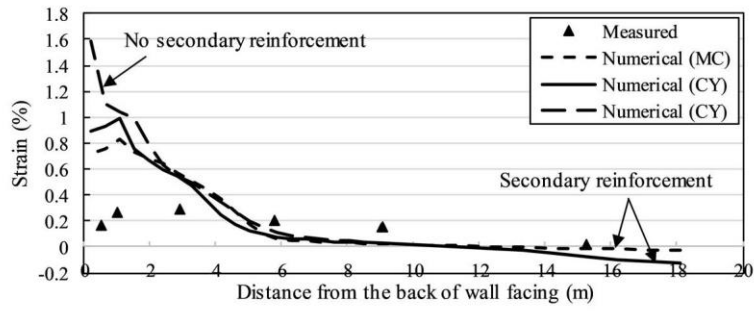
jiangfig11a



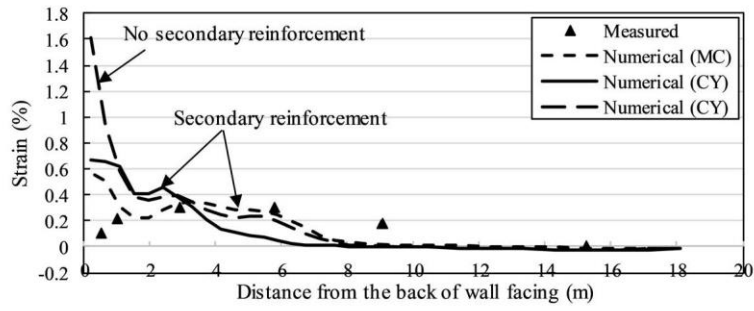
jiangfig11b



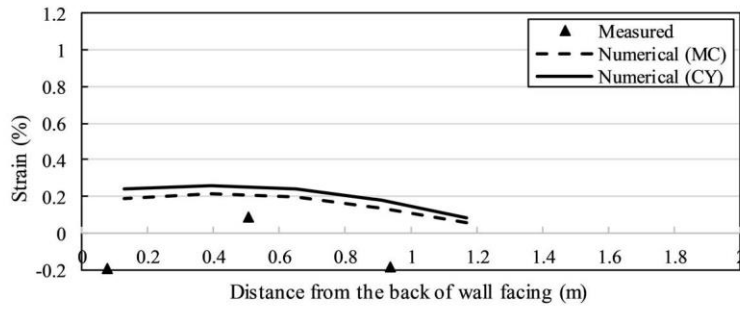
jiangfig11c



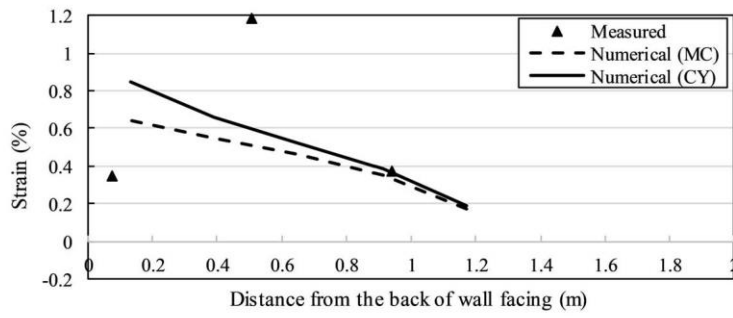
jiangfig11d



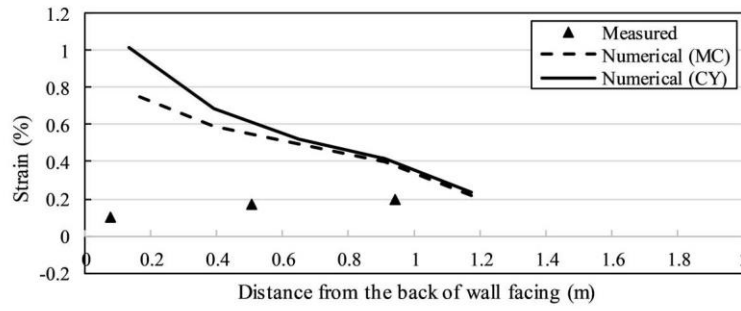
jiangfig11e



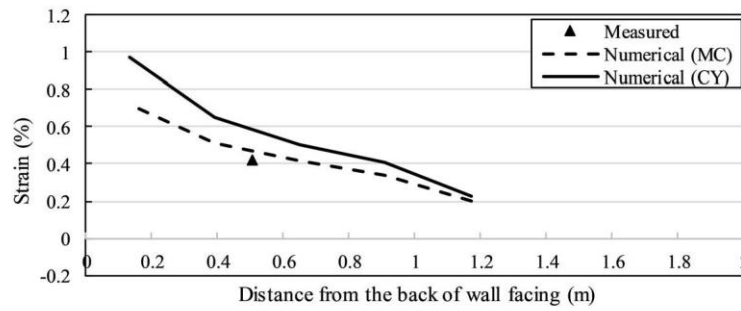
jiangfig12a



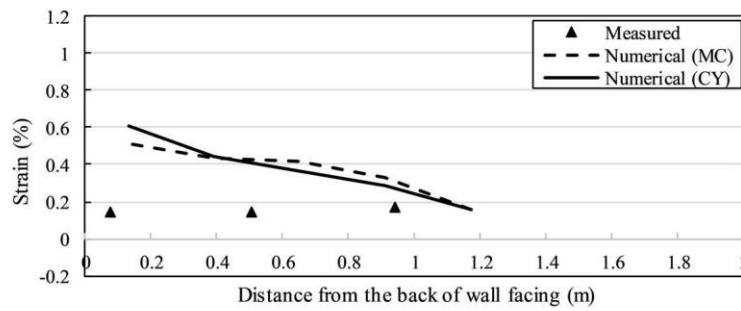
jiangfig12b



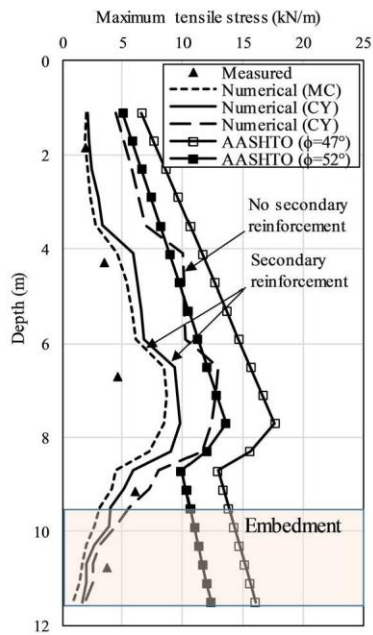
jiangfig12c



jiangfig12d



jiangfig12e



jiangfig13